Broadband and Wide Field-of-view Plasmonic Metasurface-enabled Waveplates

Zhi Hao Jiang[†], *Lan Lin*[†], *Ding Ma*[†], *Seokho Yun*,
*Douglas H. Werner**, *Zhiwen Liu**, and *Theresa S. Mayer**

Department of Electrical Engineering and Center for Nanoscale Science
The Pennsylvania State University
121 Electrical Engineering East, University Park, PA 16802 (United States)
* E-mail: dhw@psu.edu, zliu@engr.psu.edu, and tsm2@psu.edu
† These authors contributed equally to this work.

Supplementary Information

Metasurface Interference Model

Considering the multilayer structure shown in Figure 1a, by applying the boundary conditions at the interfaces between different layers, the complex reflection coefficients ($r_{ss}, r_{ps}, r_{sp}, r_{pp}$) for both *s*- and *p*-polarizations can be obtained. The time dependence is assumed to be $e^{-i\omega t}$. For an *s*- or *p*-polarized wave illuminating the nanostructure from an angle of incidence (θ_i, φ_i), the reflection coefficients for both *s*- and *p*-polarizations are expressed as

$$r_{ss} = e^{i\phi_1} \begin{vmatrix} B_1 & A_{12} & A_{13} & A_{14} \\ B_2 & A_{22} & A_{23} & A_{24} \\ B_3 & A_{32} & A_{33} & A_{34} \\ B_4 & A_{42} & A_{43} & A_{44} \end{vmatrix} \Big/ \begin{vmatrix} A_{11} & A_{12} & A_{13} & A_{14} \\ A_{21} & A_{22} & A_{23} & A_{24} \\ A_{31} & A_{32} & A_{33} & A_{34} \\ A_{41} & A_{42} & A_{43} & A_{44} \end{vmatrix}, \tag{S1a}$$

$$r_{pp} = e^{i\phi_1} \begin{vmatrix} A_{11} & C_1 & A_{13} & A_{14} \\ A_{21} & C_2 & A_{23} & A_{24} \\ A_{31} & C_3 & A_{33} & A_{34} \\ A_{41} & C_4 & A_{43} & A_{44} \end{vmatrix} \Big/ \begin{vmatrix} A_{11} & A_{12} & A_{13} & A_{14} \\ A_{21} & A_{22} & A_{23} & A_{24} \\ A_{31} & A_{32} & A_{33} & A_{34} \\ A_{41} & A_{42} & A_{43} & A_{44} \end{vmatrix}, \tag{S1b}$$

$$r_{ps} = e^{i\phi_1} \begin{vmatrix} A_{11} & B_1 & A_{13} & A_{14} \\ A_{21} & B_2 & A_{23} & A_{24} \\ A_{31} & B_3 & A_{33} & A_{34} \\ A_{41} & B_4 & A_{43} & A_{44} \end{vmatrix} \Bigg/ \begin{vmatrix} A_{11} & A_{12} & A_{13} & A_{14} \\ A_{21} & A_{22} & A_{23} & A_{24} \\ A_{31} & A_{32} & A_{33} & A_{34} \\ A_{41} & A_{42} & A_{43} & A_{44} \end{vmatrix}, \tag{S1c}$$

$$r_{sp} = e^{i\phi_1} \begin{vmatrix} C_1 & A_{12} & A_{13} & A_{14} \\ C_2 & A_{22} & A_{23} & A_{24} \\ C_3 & A_{32} & A_{33} & A_{34} \\ C_4 & A_{42} & A_{43} & A_{44} \end{vmatrix} \Bigg/ \begin{vmatrix} A_{11} & A_{12} & A_{13} & A_{14} \\ A_{21} & A_{22} & A_{23} & A_{24} \\ A_{31} & A_{32} & A_{33} & A_{34} \\ A_{41} & A_{42} & A_{43} & A_{44} \end{vmatrix}. \tag{S1d}$$

The matrix coefficients can be expressed as

$$A_{11} = \frac{\cos\theta_i \cos\varphi_i}{\eta_0} + \frac{ik_0\chi_E^y \cos\varphi_i}{2\eta_0} + \frac{ik_0\chi_M^z \sin^2\theta_i \cos\varphi_i}{2\eta_0}$$

$$A_{21} = -\frac{\cos\theta_i \sin\varphi_i}{\eta_0} - \frac{ik_0\chi_E^x \sin\varphi_i}{2\eta_0} - \frac{ik_0\chi_M^z \sin^2\theta_i \sin\varphi_i}{2\eta_0}$$

$$A_{31} = \sin\varphi_i$$

$$A_{41} = \cos\varphi_i$$

$$A_{12} = -\frac{\sin\varphi_i}{\eta_0} - \frac{ik_0\chi_E^y \cos\theta_i \sin\varphi_i}{2\eta_0}$$

$$A_{22} = -\frac{\cos\varphi_i}{\eta_0} - \frac{ik_0\chi_E^x \cos\theta_i \cos\varphi_i}{2\eta_0}$$

$$A_{32} = \cos\theta_i \cos\varphi_i + \frac{ik_0\chi_E^z \sin^2\theta_i \cos\varphi_i}{2}$$

$$A_{42} = -\cos\theta_i \sin\varphi_i - \frac{ik_0\chi_E^z \sin^2\theta_i \sin\varphi_i}{2}$$

$$A_{13} = \frac{\left(e^{i\phi_2} - r_{au}^s e^{i\phi_3}\right)\cos\theta_t \cos\varphi_i}{2\eta_d \cos\theta_i}\left[2\cos\phi_1\cos\theta_i + k_0\sin\phi_1\left(\chi_E^y + \chi_M^z \sin^2\theta_i\right)\right] - \frac{i\left(e^{i\phi_2} + r_{au}^s e^{i\phi_3}\right)\cos\varphi_i}{2\eta_0}\left[2\sin\phi_1\cos\theta_i - k_0\cos\phi_1\left(\chi_E^y + \chi_M^z \sin^2\theta_i\right)\right]$$

$$A_{23} = \frac{-\left(e^{i\phi_2} - r_{au}^s e^{i\phi_3}\right)\cos\theta_t \sin\varphi_i}{2\eta_d \cos\theta_i}\left[2\cos\phi_1\cos\theta_i + k_0\sin\phi_1\left(\chi_E^y + \chi_M^z \sin^2\theta_i\right)\right] + \frac{i\left(e^{i\phi_2} + r_{au}^s e^{i\phi_3}\right)\sin\varphi_i}{2\eta_0}\left[2\sin\phi_1\cos\theta_i - k_0\cos\phi_1\left(\chi_E^x + \chi_M^z \sin^2\theta_i\right)\right]$$

$$A_{33} = \frac{i\eta_0\left(e^{i\phi_2} - r_{au}^s e^{i\phi_3}\right)\cos\theta_t \sin\varphi_i}{\eta_d \cos\theta_i}\sin\phi_1 - \left(e^{i\phi_2} + r_{au}^s e^{i\phi_3}\right)\cos\phi_1 \sin\varphi_i$$

$$A_{43} = \frac{i\eta_0\left(e^{i\phi_2} - r_{au}^s e^{i\phi_3}\right)\cos\theta_t \cos\varphi_i}{\eta_d \cos\theta_i}\sin\phi_1 - \left(e^{i\phi_2} + r_{au}^s e^{i\phi_3}\right)\cos\phi_1 \cos\varphi_i$$

$$A_{14} = -\frac{i\left(e^{i\phi_2} + r_{au}^{p} e^{i\phi_3}\right)\cos\theta_t \sin\varphi_i}{2\eta_0 \cos\theta_i}\left[2\sin\phi_1 - k_0\cos\phi_1 \chi_E^y \cos\theta_i\right] + \frac{\left(e^{i\phi_2} - r_{au}^{p} e^{i\phi_3}\right)\sin\varphi_i}{2\eta_d}\left[2\cos\phi_1 + k_0\sin\phi_1 \chi_E^y \cos\theta_i\right]$$

$$A_{24} = -\frac{i\left(e^{i\phi_2} + r_{au}^{p} e^{i\phi_3}\right)\cos\theta_t \cos\varphi_i}{2\eta_0 \cos\theta_i}\left[2\sin\phi_1 - k_0\cos\phi_1 \chi_E^x \cos\theta_i\right] + \frac{\left(e^{i\phi_2} - r_{au}^{p} e^{i\phi_3}\right)\cos\varphi_i}{2\eta_d}\left[2\cos\phi_1 + k_0\sin\phi_1 \chi_E^x \cos\theta_i\right]$$

$$A_{34} = \frac{\left(e^{i\phi_2} + r_{au}^{p} e^{i\phi_3}\right)\cos\theta_t \cos\varphi_i}{2\cos\theta_i}\left[2\cos\phi_1 \cos\theta_i + k_0\sin\phi_1 \chi_E^z \sin^2\theta_i\right] - \frac{i\eta_0\left(e^{i\phi_2} - r_{au}^{p} e^{i\phi_3}\right)\cos\varphi_i}{2\eta_d}\left[2\sin\phi_1 \cos\theta_i - k_0\cos\phi_1 \chi_E^z \sin^2\theta_i\right]$$

$$A_{44} = \frac{\left(e^{i\phi_2} + r_{au}^{p} e^{i\phi_3}\right)\cos\theta_t \sin\varphi_i}{2\cos\theta_i}\left[-2\cos\phi_1 \cos\theta_i - k_0\sin\phi_1 \chi_E^z \sin^2\theta_i\right] + \frac{i\eta_0\left(e^{i\phi_2} - r_{au}^{p} e^{i\phi_3}\right)\sin\varphi_i}{2\eta_d}\left[2\sin\phi_1 \cos\theta_i - k_0\cos\phi_1 \chi_E^z \sin^2\theta_i\right]$$

$$B_1 = \frac{\cos\theta_i \cos\varphi_i}{\eta_0} - \frac{ik_0 \chi_E^y \cos\varphi_i}{2\eta_0} - \frac{ik_0 \chi_M^z \sin^2\theta_i \cos\varphi_i}{2\eta_0}$$

$$B_2 = -\frac{\cos\theta_i \sin\varphi_i}{\eta_0} + \frac{ik_0 \chi_E^x \sin\varphi_i}{2\eta_0} + \frac{ik_0 \chi_M^z \sin^2\theta_i \sin\varphi_i}{2\eta_0}$$

$$B_3 = -\sin\varphi_i,\ B_4 = -\cos\varphi_i$$

$$C_1 = \frac{\sin\varphi_i}{\eta_0} - \frac{ik_0 \chi_E^y \cos\theta_i \sin\varphi_i}{2\eta_0}$$

$$C_2 = \frac{\cos\varphi_i}{\eta_0} - \frac{ik_0 \chi_E^x \cos\theta_i \cos\varphi_i}{2\eta_0}$$

$$C_3 = \cos\theta_i \cos\varphi_i - \frac{ik_0 \chi_E^z \sin^2\theta_i \cos\varphi_i}{2}$$

$$C_4 = -\cos\theta_i \sin\varphi_i - \frac{ik_0 \chi_E^z \sin^2\theta_i \sin\varphi_i}{2}$$

(S2)

where $\phi_1 = k_0 t_m \cos\theta_i/2$, $\phi_2 = n_d k_0 t_m \cos\theta_t/2$, and $\phi_3 = n_d k_0 (2t_d + t_m/2)\cos\theta_t$. It should be noted that in Eq. (S1), the cross-polarization reflection coefficients r_{ps} and r_{sp} have the same value due to reciprocity. These two coefficients also vanish when the plane of incidence coincides with the *x*-*z* ($\varphi_i = 0°$) or *y*-*z* ($\varphi_i = 90°$) plane, *i.e.* a plane determined by two of the three optical axes of the metasurface. This model can also be used for the tri-layer nanostructured

waveplates. Using the extracted effective surface polarizability tensors ($\bar{\bar{\chi}}_E$ and $\bar{\bar{\chi}}_M$) of the top nanorod array, the reflection coefficients of the tri-layer nanostructure under illumination of light with an arbitrary angle of incidence and polarization can be evaluated.

To validate this method, here we compare the reflection coefficients r_{ss}, r_{pp}, and $r_{sp}(= r_{ps})$ of the metasurface half-wave plate nanostructure (see Figure 3 in the main text) predicted by the metasurface interference model using the extracted surface polarizability tensor parameters of the nanorod array to those calculated by full-wave simulations of the entire trilayer nanostructure. Here an *s*-polarized and *p*-polarized plane wave are assumed to be illuminating the nanostructure at an incident angle of $(\theta_i, \varphi_i = 30°)$. The reflection coefficients r_{ss}, $r_{sp}(= r_{ps})$, and r_{pp} at various elevation angles (0°, 20°, 40°, and 60°) calculated using the metasurface interference model as described above are shown in Figure S1, which agree almost perfectly with results obtained by simulating the entire tri-layer nanostructure using the HFSS full-wave solver (also plotted in Figure S1). This indicates that the metasurface interference model can be used to evaluate the optical properties of the tri-layer nanostructure considered here.

This interference model not only sheds light on how the tri-layer nanostructure, which behaves as a metasurface G-T interferometer, responds to incident light but also greatly increases the speed of the design process. In particular, for a specific nanostructure with a certain top nanorod array metasurface, only three full-wave unit cell simulations of the nanorod residing on a SiO_2 half-space are required. These include two *s*-polarized incident waves with different incident angles and one *p*-polarized wave at an arbitrary oblique angle of incidence. The optical response of a class of tri-layer nanostructures having the same top metasurface layer but different thickness values for the SiO_2 spacer and the bottom gold layer can be evaluated almost

instantaneously, even over a wide angular range. Due to the fact that in our case the interference plays an important role and the spacer thickness thus becomes a critical design parameter, the metasurface interference model can be utilized to dramatically improve the efficiency of the design process.

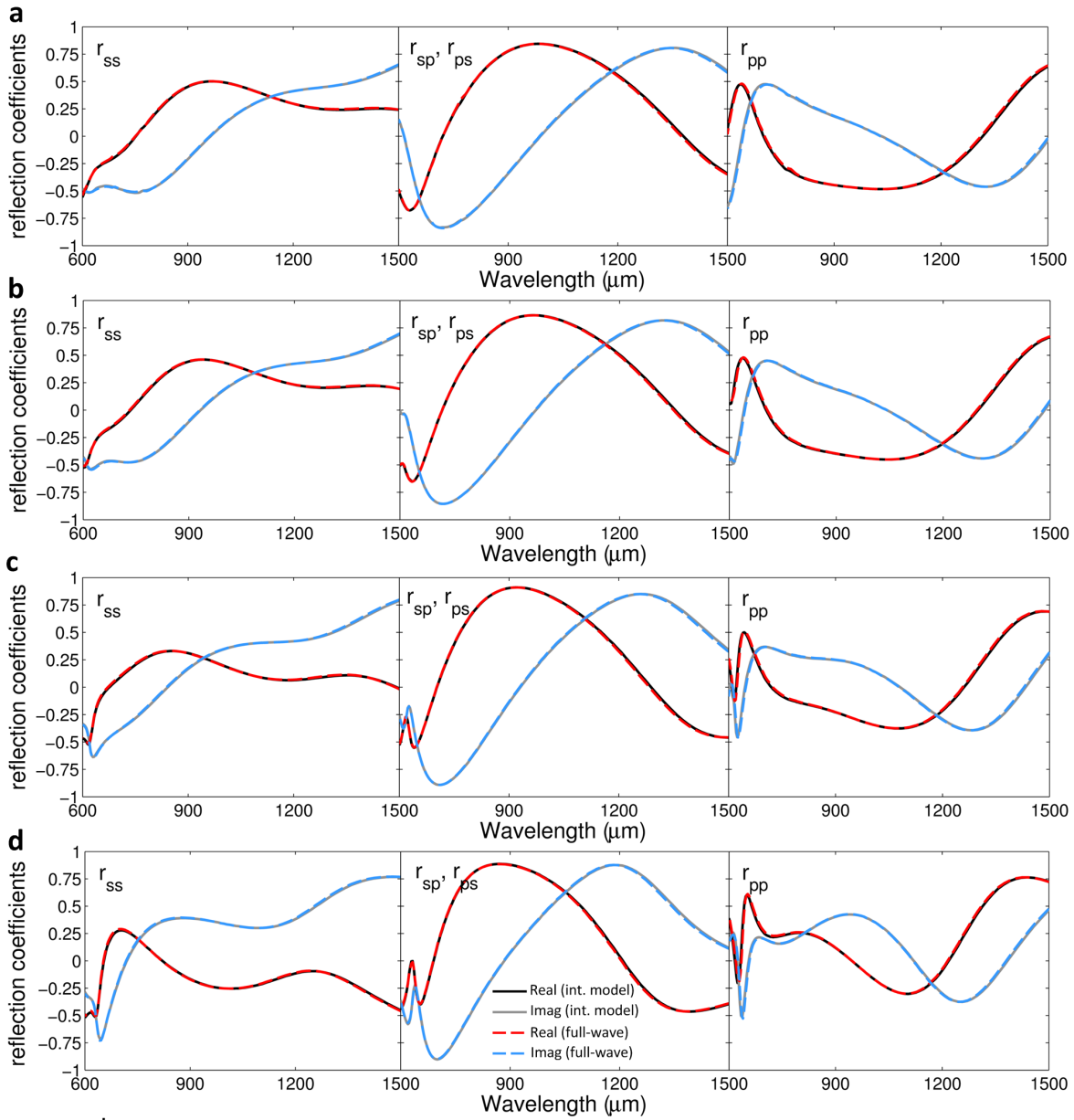

Figure S1 | Reflection coefficients of trilayer nanostructure calculated using metasurface interference model and full-wave solver. Real and imaginary parts of the reflection coeffcients r_{ss}, $r_{sp}(= r_{ps})$, and r_{pp} calculated using the metasurface interference model and a full-wave solver with an angle of incidence of **a)** ($\theta_i = 0°$, $\varphi_i = 30°$), **b)** ($\theta_i = 20°$, $\varphi_i = 30°$), **c)** ($\theta_i = 40°$, $\varphi_i = 30°$), and **d)** ($\theta_i = 60°$, $\varphi_i = 30°$).

Scattering of Single and Coupled Nanorod at Oblique Incidence Angles

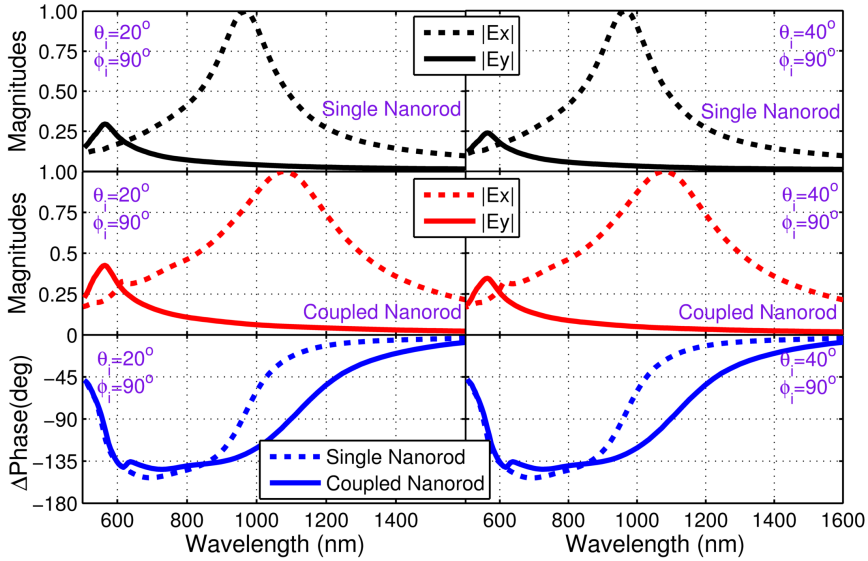

Figure S2 | Anisotropic scattering of a single and coupled nanorod pair at oblique angles of incidence with incident wave in the *y*-*z* plane. Scattering field magnitudes (normalized) and phases of the single and coupled nanorod pair. Two plane waves, one with its *E*-field polarized in the *x*-direction and the other with its *H*-field polarized in the *x*-direction, were employed to excite the nanorod at an incident angle of ($\theta_i = 20°,\ 40°$ and $\varphi_i = 90°$).

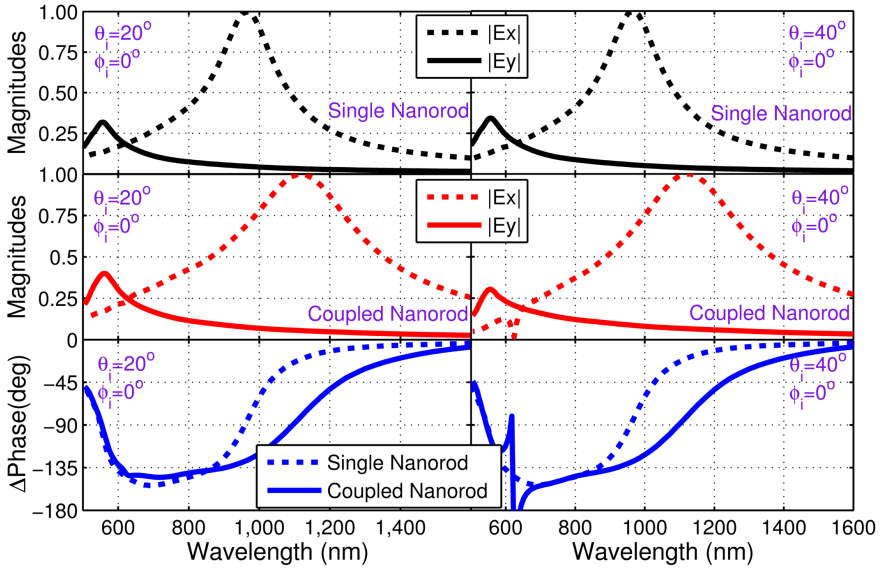

Figure S3 | Anisotropic scattering of a single and coupled nanorod pair at oblique angles of incidence with incident wave in *x*-*z* plane. Scattering field magnitudes (normalized) and phases of the single and coupled nanorod pair. Two plane waves, one with its *E*-field polarized in the *y*-direction and the other with its *H*-field polarized in the *y*-direction, were employed to excite the nanorod at an incident angle of ($\theta_i = 20°, 40°$ and $\varphi_i = 0°$).

Nanorod Array Effective Surface Polarizability Extraction

Due to the fact that both the array periodicity and the size of the nanorod are much smaller than the wavelength of interest, the single-layer nanorod array can be used to effectively synthesize the anisotropic homogeneous metasurface characterized by two uniaxial surface polarizability tensors $\bar{\bar{\chi}}_E$ and $\bar{\bar{\chi}}_M$. As shown in Figure 1a, in order to account for the wave retardation caused by the finite thickness of the nanorods, two thin air layers with a thickness of $t_m/2$ are added above and below the metasurface which is assumed to have a zero thickness. Since there is no magnetic material being used, the surface polarizability tensors of the homogenized metasurface can be simplified to have the forms of $\bar{\bar{\chi}}_E = [\chi_E^x, \chi_E^y, \chi_E^z]$ and $\bar{\bar{\chi}}_M = [0, 0, \chi_M^z]$. These four parameters can be retrieved by the complex transmission and reflection coefficients calculated for three incident waves - two *s*-polarized waves with different incident angles and one *p*-polarized wave at oblique incidence.

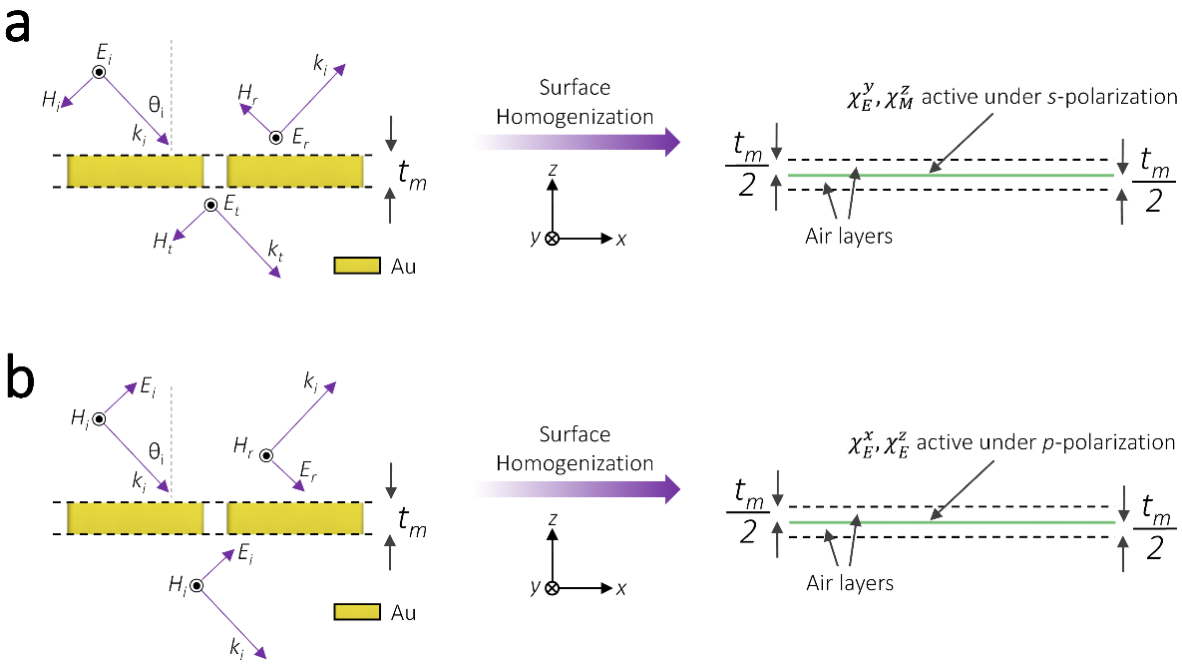

Figure S4 | Surface polarizability extraction using complex transmission and reflection coefficients. **a)** Extracting χ_E^y and χ_M^z using two *s*-polarized illuminating waves - one at normal incidence and one at oblique incidence. **b)** Extracting χ_E^x and χ_E^z using one *p*-polarized illuminating wave at oblique incidence.

As shown in Figure S4a, χ_E^y and χ_M^z are active when the nanorod array is illuminated by a *s*-polarized wave and can be extracted by

$$\chi_E^y(\lambda) = \frac{i\lambda}{\pi}\frac{1-t(0°,\lambda)e^{-i2\pi t_m/\lambda}}{t(0°,\lambda)e^{-i2\pi t_m/\lambda}} \tag{S3a}$$

$$\chi_M^z(\lambda) = \frac{1}{\sin^2(\theta_i)}\left(\chi_E^y(\lambda) - i\frac{\lambda\cos(\theta_i)}{\pi}\right)\frac{1-t(\theta_i,\lambda)e^{-i2\pi\cos(\theta_i)t_m/\lambda}}{t(\theta_i,\lambda)e^{-i2\pi\cos(\theta_i)t_m/\lambda}}, \tag{S3b}$$

where $t(0°,\lambda)$ is the normal incidence complex transmission coefficient, while $t(\theta_i,\lambda)$ is the oblique incidence complex transmission coefficient of the infinite nanorod array in free space. It should be noted that since χ_M^x is zero, the tangential electric field at the two sides of the metasurface is continuous. Consequently, the transmission and reflection coefficients satisfy the condition $t(\theta_i,\lambda) - r(\theta_i,\lambda) = 1$.

Similarly, as Figure S4b shows, χ_E^x and χ_E^z are active when the nanorod array is illuminated by a *p*-polarized wave and can be extracted by

$$\chi_E^x = \frac{i}{\cos^2(\theta_i)}\frac{\lambda\cos(\theta_i)}{\pi}\frac{[t(\theta_i,\lambda)+r(\theta_i,\lambda)]e^{-i2\pi\cos(\theta_i)t_m/\lambda}-1}{[t(\theta_i,\lambda)+r(\theta_i,\lambda)]e^{-i2\pi\cos(\theta_i)t_m/\lambda}+1} \tag{S4a}$$

$$\chi_E^z = \frac{i}{\sin^2(\theta_i)}\frac{\lambda\cos(\theta_i)}{\pi}\frac{[t(\theta_i,\lambda)-r(\theta_i,\lambda)]e^{-i2\pi\cos(\theta_i)t_m/\lambda}-1}{[t(\theta_i,\lambda)-r(\theta_i,\lambda)]e^{-i2\pi\cos(\theta_i)t_m/\lambda}+1}, \tag{S4b}$$

where $t(\theta_i,\lambda)$ and $r(\theta_i,\lambda)$ are the oblique incidence complex transmission and reflection coefficients of the infinite nanorod array in free space, respectively. It should be noted that since χ_E^x is non-zero, unlike the case for the *s*-polarization, then the condition $t(\theta_i,\lambda) - r(\theta_i,\lambda) = 1$ is not satisfied which means that both the tangential electric and magnetic fields have discontinuities across the metasurface. However, because χ_M^y is zero, the transmission and reflection coefficients for *only one* oblique incidence angle are enough for extracting both χ_E^x and χ_E^z.

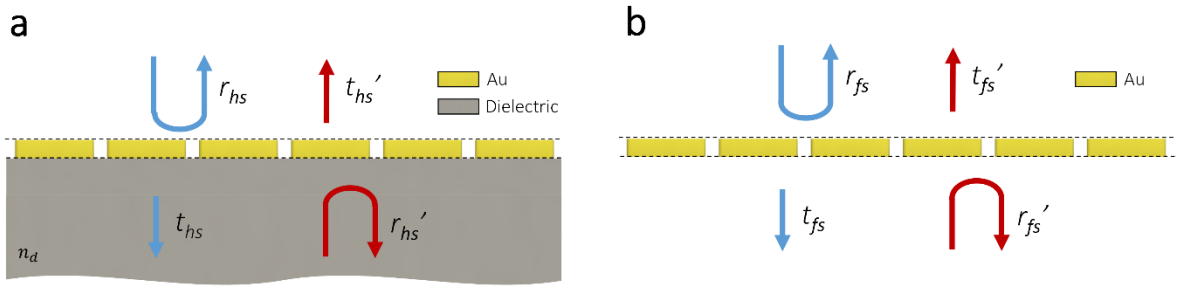

Figure S5 | Nanorod array on a dielectric half space. Transmission and reflection coefficients of **a)** a nanorod array on the dielectric half space having an index of n_d are transformed to transmission and reflection coefficients of **b)** a nanorod array in free space.

In order to take into account the loading effect of the dielectric spacer (having an index of n_d) on the nanorod array, the surface property extraction procedure is modified. Since the nanorod array is electrically thin, the impact of the dielectric spacer on the nanorods is limited only in the near field. Hence, the dielectric spacer can be considered as a half space for extracting the equivalent polarizability tensor parameters of the metasurface for the on-dielectric nanorod array, as shown in Figure S5. In order to account for the different impedance values of the top air and bottom dielectric half spaces, the transmission and reflection coefficients calculated for light incident from both the air and the substrate sides are scaled by referencing them to the characteristic impedance of free space using the scattering transfer matrix, or T matrix, technique. First, the T matrix of the nanorod array on the dielectric half space is transformed from the transmission and reflection coefficients obtained using full-wave unit cell simulations as

$$T_{total}^{s(p)}(\theta_i,\lambda) = \frac{1}{t_{hs}(\theta_i,\lambda)}\begin{bmatrix} 1 & -r_{hs}'(\theta_i,\lambda) \\ r_{hs}(\theta_i,\lambda) & -r_{hs}(\theta_i,\lambda)r_{hs}'(\theta_i,\lambda) + t_{hs}(\theta_i,\lambda)t_{hs}'(\theta_i,\lambda) \end{bmatrix}. \quad \text{(S5)}$$

The T matrix of the nanorod array layer can then be calculated by

$$T_{np}^{s(p)}(\theta_i,\lambda) = \left(T_{hs}^{s(p)}\right)^{-1}(\theta_i,\lambda)\cdot T_{total}^{s(p)}(\theta_i,\lambda)\,. \quad \text{(S6)}$$

where $T_{hs}^{s(p)}$ is the matching matrix corresponding to the interface between dielectric and free space, which can be written as

$$T_{hs}^{s}(\theta_i,\lambda)=\begin{bmatrix}\frac{n_d\cos(\theta_t)+\cos(\theta_i)}{2n_d\cos(\theta_t)} & \frac{n_d\cos(\theta_t)-\cos(\theta_i)}{2n_d\cos(\theta_t)}\\ \frac{n_d\cos(\theta_t)-\cos(\theta_i)}{2n_d\cos(\theta_t)} & \frac{n_d\cos(\theta_t)+\cos(\theta_i)}{2n_d\cos(\theta_t)}\end{bmatrix} \tag{S7a}$$

for *s*-polarization, and

$$T_{hs}^{p}(\theta_i,\lambda)=\begin{bmatrix}\frac{n_d\,cos(\theta_i)+cos(\theta_t)}{2n_d\,cos(\theta_t)} & \frac{n_d\,cos(\theta_i)-cos(\theta_t)}{2n_d\,cos(\theta_t)}\\ \frac{n_d\,cos(\theta_i)-cos(\theta_t)}{2n_d\,cos(\theta_t)} & \frac{n_d\,cos(\theta_i)+cos(\theta_t)}{2n_d\,cos(\theta_t)}\end{bmatrix} \tag{S7b}$$

for *p*-polarization, respectively, with $\theta_t=\sin^{-1}(\sin(\theta_i)/n_d)$ where θ_i is the angle of incidence. Finally, the transmission and reflection coefficients of the nanorod array alone can be obtained from the following relation

$$\begin{bmatrix}r_{fs}(\theta_i,\lambda) & t_{fs}{}'(\theta_i,\lambda)\\ t_{fs}(\theta_i,\lambda) & r_{fs}{}'(\theta_i,\lambda)\end{bmatrix}=\begin{bmatrix}\frac{T_{np21}(\theta_i,\lambda)}{T_{np11}(\theta_i,\lambda)} & T_{np22}(\theta_i,\lambda)-\frac{T_{np12}(\theta_i,\lambda)T_{np21}(\theta_i,\lambda)}{T_{np11}(\theta_i,\lambda)}\\ \frac{1}{T_{np11}(\theta_i,\lambda)} & -\frac{T_{np12}(\theta_i,\lambda)}{T_{np11}(\theta_i,\lambda)}\end{bmatrix}. \tag{S8}$$

These coefficients can then be used to extract the surface polarizability tensor parameters through the procedure presented earlier.

Simulated and Measured Results for Metasurface Half-wave Plate

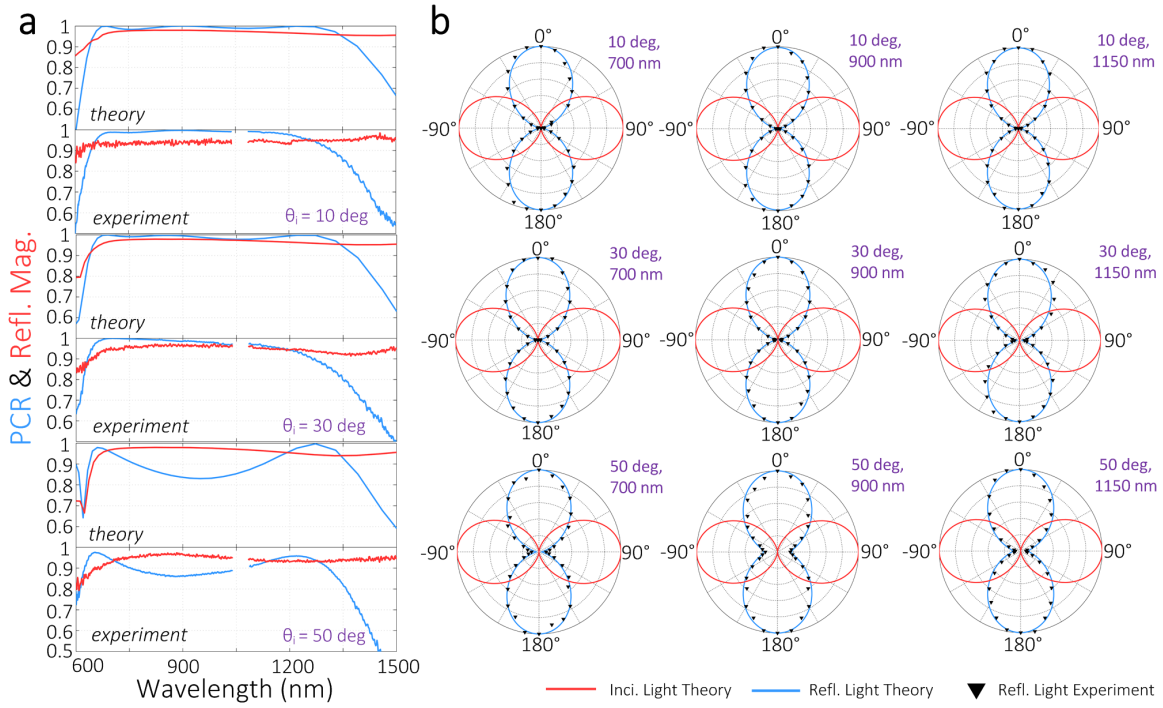

Figure S6 | Additional simulated and measured results of broadband and wide-angle metasurface-enabled half-wave plate. a) Theoretically predicted and experimentally measured polarization conversion ratio (PCR) and reflection magnitude (Refl. Mag.) as a function of wavelength at different angles of incidence (10°, 30°, 50°). **b)** Theoretically predicted and experimentally measured polarization state in the plane perpendicular to the wave vector at 700, 900, and 1150 nm for different angles of incidence (10°, 30°, 50°).

Simulated and Measured Results for Metasurface Quarter-wave Plate

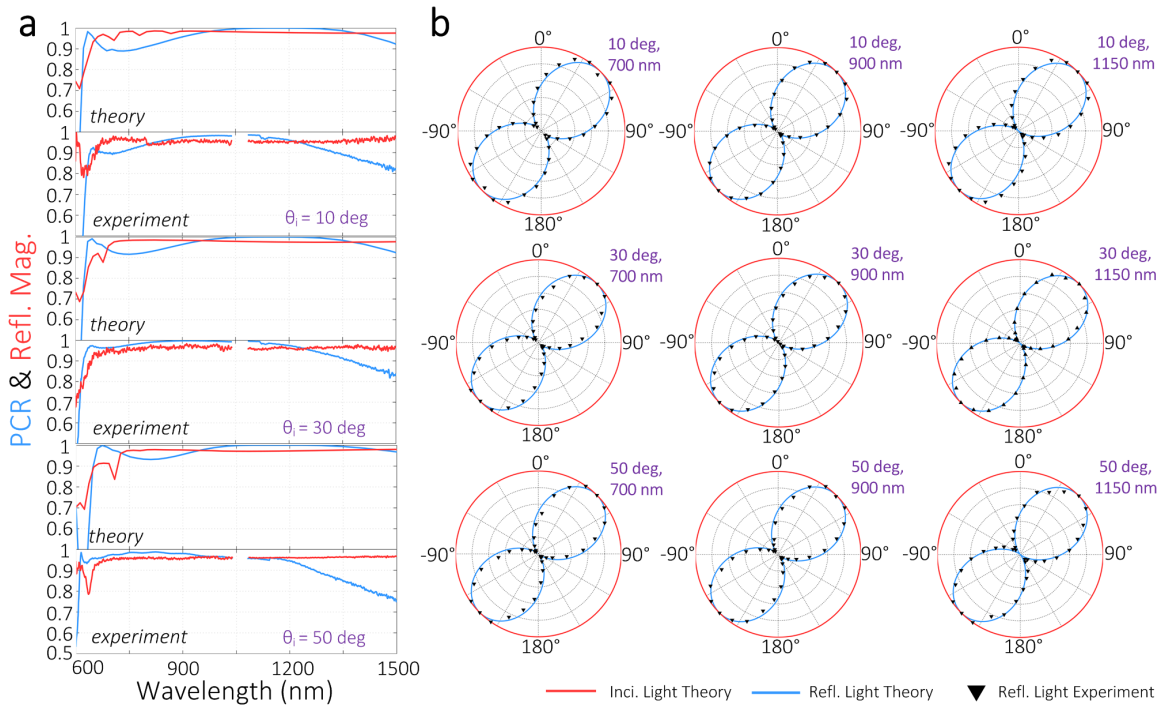

Figure S7 | Additional simulated and measured results of broadband and wide-angle metasurface-enabled quarter-wave plate. a) Theoretically predicted and experimentally measured polarization conversion ratio (PCR) and reflection magnitude (Refl. Mag.) as a function of wavelength at different angles of incidence (10°, 30°, 50°). **b)** Theoretically predicted and experimentally measured polarization state in the plane perpendicular to the wave vector at 700, 900, and 1150 nm for different angles of incidence (10°, 30°, 50°).

Schematics of Optical Characterization of the Meta-waveplates

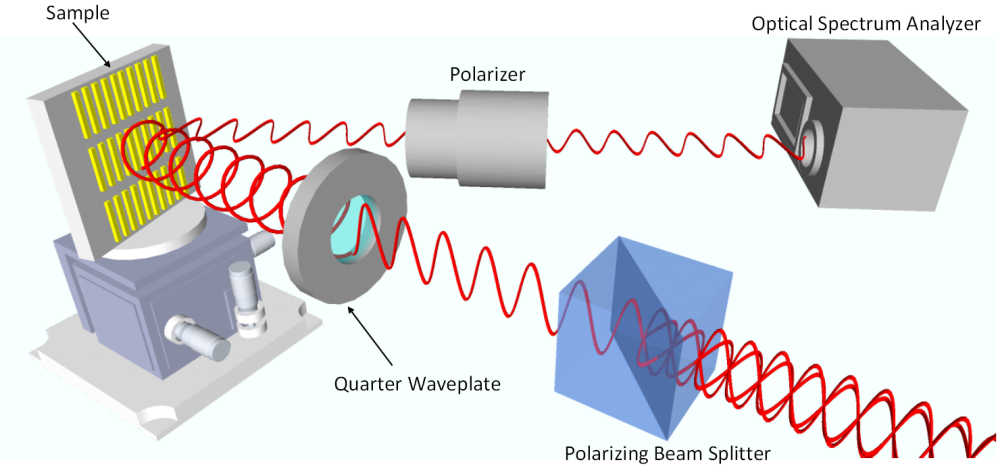

Figure S8 | Optical setup for sample characterization. For the metasurface quarter-wave plate, a conventional optical quarter-wave plate was used to generate circularly polarized incident light. For the metasurface half-wave plate, the conventional optical quarter-wave plate was removed, and the sample was rotated by 45°.